

Observations of Binder Jetting Defect Formation Using High-Speed Synchrotron X-Ray Imaging

Jacob Lawrence¹, Colton Inkley¹, Kamel Fezzaa², Samuel J. Clark², Nathan B. Crane¹

¹Department of Mechanical Engineering, Brigham Young University, Provo, UT, 84602, USA

²X-ray Science Division, Advanced Photon Source, Argonne National Laboratory, Argonne, IL, 60439, USA

Abstract

The Binder Jetting (BJ) process is capable of producing parts at high speeds from a variety of materials, but performance is limited by defects in the final parts. An improved understanding of fundamental phenomena in the printing process is needed to understand the source of these defects. This work presents initial findings from high-speed imaging of the BJ process using synchrotron X-rays. High-speed X-ray imaging allows for direct observation of key physical mechanisms in the printing process that may introduce defects including binder droplet impact on the powder bed, powder rearrangement below and above the powder bed surface, and balling formation. Testing was performed with multiple materials and droplet spacings to compare the effect on observed phenomena. Multiple lines were printed on packed and loose powder beds to further explore factors that affect defect formation and to better simulate industrially relevant conditions.

Keywords: Binder Jetting, Synchrotron X-ray Imaging, Binder-Powder Interaction, Print Processing Parameters, Metal

Introduction

Binder jetting (BJ) is an additive manufacturing (AM) process that uses ink jet printing technology to make 3D objects using a powder feedstock [1]. As with other powder bed AM techniques, powder is typically deposited on the build surface and rolled flat to a desired thickness. In BJ, an inkjet printhead then selectively deposits a liquid binder glue onto the powder bed, binding the particles together in the desired pattern. This process is repeated layer-by-layer to create stacked cross sections in the shape of the part to be printed. This “green” part can then be removed from the unbound powder and used directly in the case of bound sand used for sand casting or for other materials sintered or infiltrated to achieve final part properties [2].

As an AM process, BJ benefits from the ability to produce parts with high complexity, reduce lead times for custom parts, and enable on-demand production. Beyond the benefits shared among most AM processes, BJ has distinct advantages. Like other powder bed AM processes, the unbound powder in the supports parts during printing removing the need for printed supports, but in contrast to powder bed fusion (PBF) processes, minimal heat is required during the BJ process [3]. This reduces cost and power requirements for the printer itself and reduces residual stresses often present in PBF produced parts by isolating the heating to a single sintering stage. Additionally, BJ is capable of printing nearly any powdered feedstock given the powder has adequate spreading and wetting properties. BJ is commonly used to print metal powders [4], but can also print ceramics such as alumina, silica, and even sand for use as a mold for sand casting [5-8]. Furthermore, BJ offers comparatively fast build rates, as many nozzles can be used together to accelerate printing, and parts can be tightly stacked in the build volume.

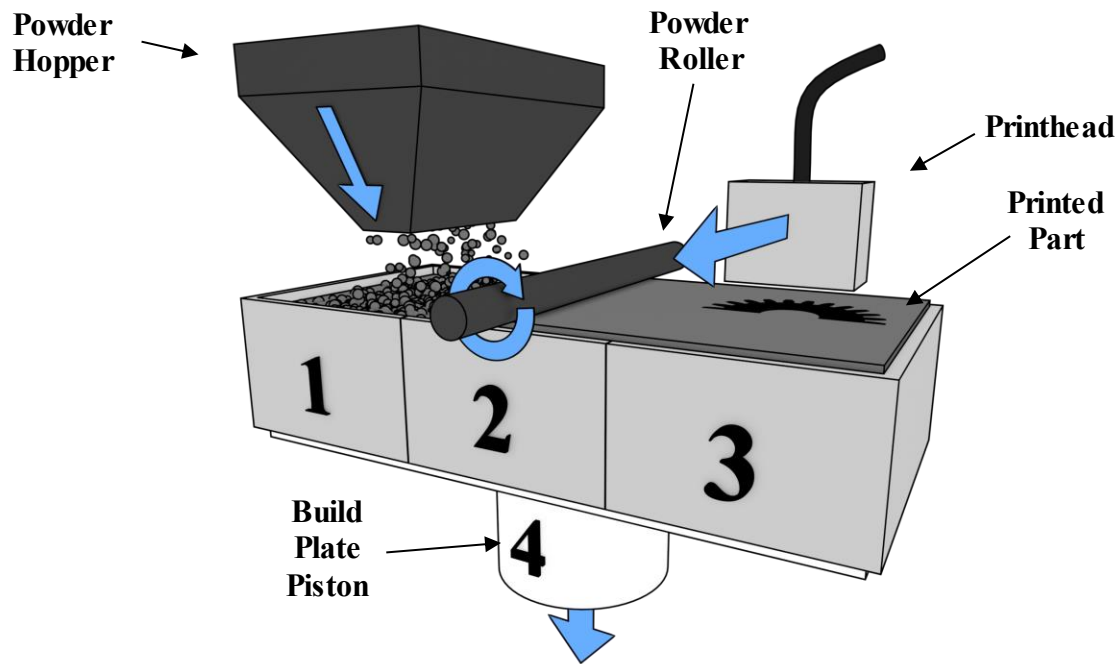


Figure 1. The basic binder jetting process includes 4 steps: 1) Deposit powder, 2) Roll powder layer, 3) Print desired pattern with inkjet printhead and 4) Lower build platen and repeat.

As with other AM processes, understanding of relevant process parameters in BJ is critical to maximize quality and material properties in printed parts. Given the relatively recent advent of and interest in BJ, understanding of governing physical phenomena during the printing process is still limited. A model for the binder saturation of the powders was proposed by Miyanaji, et al. [9] and Bai et al. proposed methods of evaluating binder/powder interactions [10]. These interactions are sensitive to many parameters including droplet size, droplet spacing, printing frequency, and moisture levels [11-13]. The complex interaction of the binder droplet with the powder bed can induce disturbances that cause print defects that may persist through the sintering process [12]. Residual porosity creates a part with inferior material properties. Observing these interactions poses a challenge as both high spatial and temporal resolutions are needed to observe droplet impact and powder rearrangement. Additionally, a significant amount of powder rearrangement that may cause defect formation occurs below the powder bed surface making *in situ* optical observation difficult. To better observe the fundamental phenomena of the BJ process, testing was conducted using high-speed synchrotron X-ray imaging. Synchrotron X-ray imaging allows for direct *in situ* observation of phenomena above and below the powder bed with high temporal resolution. Parab, et al. [14] has previously used synchrotron X-ray imaging to study the printing of single lines into powder. They observed that there was significant powder ejection during printing and that the powder was disturbed a significant distance below the surface. They characterized powder ejection and subsurface interaction depth by printing single lines in a variety of powder bed materials and found that normalized interaction depth decreased with increasing particle size. Comparing particle shapes, they also found that spherical particles experienced more particle ejection where irregularly shaped particles experienced more subsurface interaction. However, the effect of varying droplet was not explored and recent studies show that single lines are not a good indicator of BJ printing results [12]. Additionally, these powder beds were not packed as is typical in BJ.

Simulation of powder-droplet interactions is still in the early stages. The high speed of these interactions and the complexity of the two-phase flow and powder motion during impact, and the wide temporal range of key phenomena make this computationally demanding. Much of the simulations of droplet-powder impact to-date utilize simplifying assumptions such as a fixed powder bed and are limited to small numbers of interacting droplets that cannot account for the complexity of interactions in BJ printing [15-17].

In this work, a new system was fabricated for high-speed synchrotron X-ray imaging to enable more realistic printing conditions. The custom system was constructed to be capable of printing multiple lines in loose or rolled powder bed samples with a variety of materials. Droplet spacing was varied during testing to study the effect on observed phenomena. Initial analysis of these experiments reveals observations made possible through high-speed X-ray imaging that will give insight into binder-powder interaction in the BJ process. The high-speed X-ray footage enables observation of binder droplet interaction with the powder bed, powder rearrangement above and below the powder bed surface, as well as powder agglomerate formation. An additional synchronized optical high-speed camera was used to contextualize the images captured with the X-ray camera. Further analysis of these experiments will provide insight into the fundamental phenomena that drive the BJ process, which will help develop techniques to optimize the process for improved part quality.

Process

Testing was performed at beamline 32-ID-B at the Advanced Photon Source (APS), Argonne National Laboratory. A diagram of the experimental setup is shown in Figure 2. A custom laboratory-scale BJ platform was used for all experiments. The printer was designed with an open format optimized for X-ray and optical imaging. The printer was able to print on loose and rolled powder beds. Figure 2 depicts a glassy carbon sample holder that was used to contain a loose powder bed. The loose powder beds were prepared by manually depositing powder in the glassy carbon sample holders that had channel widths varying from 400 μm to 800 μm . The powder was then scraped with a blade to obtain a flat powder bed surface. Polyimide film tape was wrapped around the edges of the sample holder to prevent powder from falling out of the edges. Rolled powder beds were prepared by manually depositing powder on and around a 500 μm wide pillar that was either raised for imaging or the surrounding powder manually removed to allow for X-ray transmission through the material.

Control software for the printer enabled control over key process parameters including jetting droplet spacing and frequency, both being important parameters that have an impact on binder saturation and hence final part quality [11]. The printer was used to print lines in the powder bed both perpendicular and parallel to the direction of the X-ray source. The printer was also used to print consecutive lines in a single powder bed printed at a desired spacing between the lines. A high-speed output trigger signal was sent from the printer 100 milliseconds before the jetting nozzle reached the desired imaging position to synchronize the X-ray shutters and high-speed cameras.

Key process parameters were selected to explore their effect on observed physical phenomena. Multiple materials were tested including Stainless Steel 316L, fine and coarse glass beads, and alumina. Droplet and line spacings were varied from 15 μm to 150 μm . Jetting frequency

was predominately set at 1000Hz, and traverse rate was varied to obtain different droplet spacings. Consecutive lines were printed on loose and rolled powder beds to simulate industrially relevant conditions.

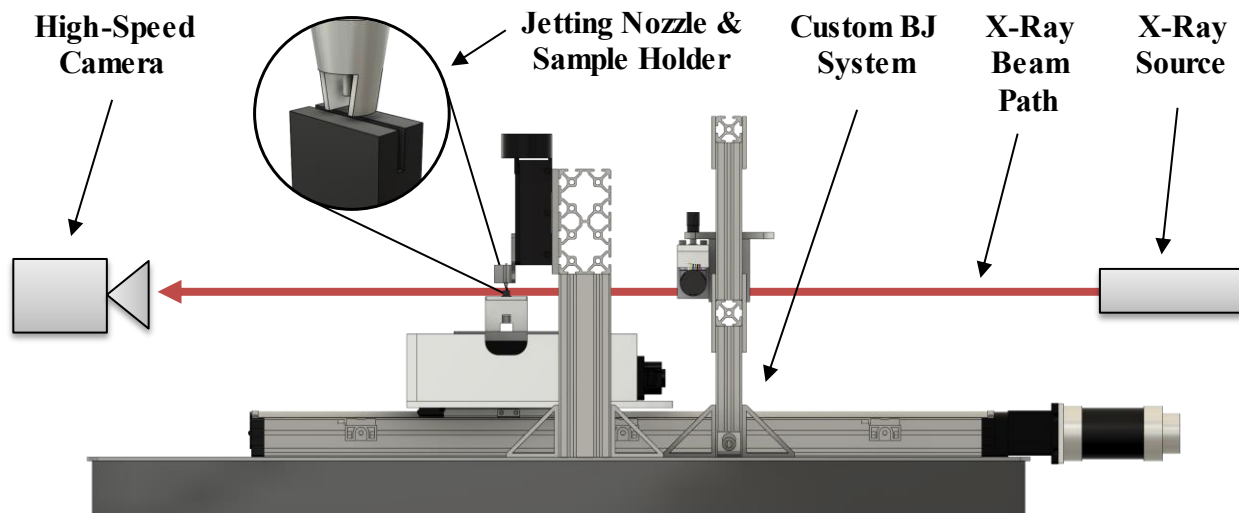


Figure 2. Printer configuration.

Jetting Setup and Printing Parameters

Testing was performed with a MJ-ABP-01 MicroFab piezo-electric inkjet nozzle with a $30\mu\text{m}$ nozzle orifice. The inkjet nozzle is a single nozzle drop-on-demand printhead that was controlled by a MicroFab JetDrive III. ExOne BA005 Aqueous Binder was used for printing. An IDS UI-3370CP-M-GL Rev. 2 USB camera with an Edmund Optics VZM 1000i Zoom Imaging Lens was pointed at the jetting nozzle backlit by a controllable strobing LED to estimate droplet velocity. The LED was set to strobe at the nozzle jetting frequency and strobe offset could be adjusted during image capture to generate a sequence of images showing droplets at specific times after nozzle actuation. A MATLAB script was used calculate droplet velocity by tracking droplets present in the captured image sequence. Average droplet volume was obtained by jetting continuously into a sample container at 1000Hz for three minutes. The sample container was weighed, and average droplet volume could be estimated assuming spherical droplets. Before testing, jetting voltage was adjusted to obtain a measured droplet velocity of 7.5 ± 0.1 m/s. Droplet volume was measured to range from 52-63 picoliters. Measurement accuracy was limited by the resolution of the scale available at APS (10 mg) against a total mass of printed binder of 120 mg.

Results shown in this study were printed on powder beds of stainless steel 316L and soda-lime glass microsphere powder. The stainless steel 316L powder had a volume average particle diameter ($Dv50$) of $10.0\mu\text{m}$ ($Dv10$ of $3.92\mu\text{m}$ and $Dv90$ of $22.0\mu\text{m}$). The soda-lime glass spheres ranged in size from $1\text{-}20\mu\text{m}$. Both are spherical powders. Sample holders were weighed before and after depositing powder to get an estimate of powder density. Stainless steel samples were measured to have an average density of 50% and soda-lime glass microsphere samples were measured to have an average density of 40%.

High-Speed Imaging

The high-speed X-ray images were recorded with a Photron Limited Photron SA-Z. Images were recorded at 50,000 frames per second. Optical high-speed footage was recorded using an Integrated Design Tools (IDT) NX8-S2. Optical high-speed images were recorded at 10,000 frames per second and frames were synchronized with the Photron camera. The printer was placed such that the X-ray source propagated through the length of the center of the printer, passed through the sample, and was converted to visible light for imaging using a single crystal $Lu_3Al_5O_{12}:Ce$ scintillator. Complete details of the X-ray beam and imaging camera are described by Parab, et al. [14]. The optical high-speed camera was placed above the sample at angle to observe the same region as the X-ray camera while not obstructing the path of the X-ray beam. A Veritas Constellation 120E was used to light the sample for optical high-speed imaging.

X-Ray Imaging

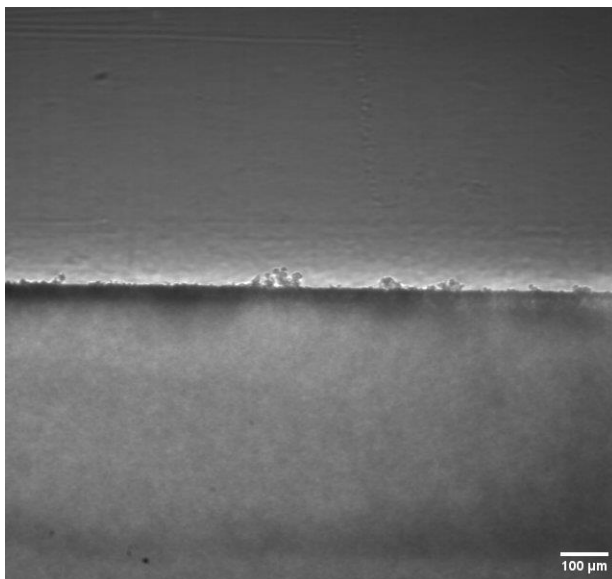


Figure 3. A loose stainless steel sample before printing as recorded on the Photron SA-Z.

The Photron SA-Z recorded tests as a series of 16-bit grayscale images. A sample frame showing a loosely packed stainless steel powder sample before printing is shown in Figure 3. A region of interest of 1.27mm by 1.19mm was chosen with a scale of 1.98 μ m per pixel. The grayscale value in the image corresponds to the amount of the X-ray beam transmitted through the sample. The image exposure was set by controlling the imaging sensor exposure time and setting the X-ray beam intensity by adjusting the gap distance on the short-period (18mm) undulator. Increasing gap distance results in overall lower beam intensity. Both the gap distance and camera exposure time were adjusted for each material tested to accommodate the specific X-ray attenuation of the material. With a beam energy of \sim 24,500 eV and typical sample thickness of \sim 400 μ m, a silica (SiO_2) glass powder allows for transmission of \sim 90% of the X-ray beam, where iron (Fe) based powders have a transmission of only \sim 1%.

When testing materials with low X-ray transmission such as stainless steel 316L, a steel attenuator strip was placed in the path of the X-ray beam and aligned with the interface between

the powder bed surface and the air above. In the perspective of the X-ray imaging camera, the attenuator strip covered the space above the powder bed. The attenuator strip was used to match dynamic ranges of powder bed and the space above to avoid saturating the imaging sensor while still having sufficient X-ray intensity to penetrate the sample. This allowed for simultaneous observation of phenomena above and below the powder bed surface. A slight misalignment between the attenuator strip and the powder bed surface can be observed in a few of the tests. This misalignment presents as a light region immediately above the powder bed surface if the attenuator is positioned too high or a dark region immediately below the powder bed surface if the attenuator is positioned too low as illustrated in Figure 4.

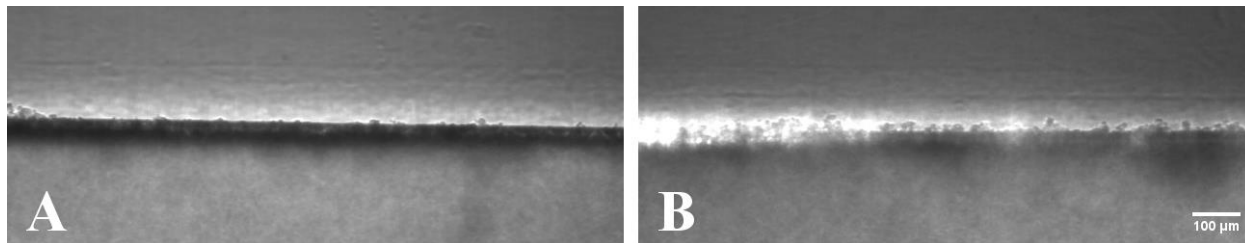


Figure 4. A) Attenuator strip positioned too low, B) Attenuator strip positioned too high.

Optical Imaging

Supplementary optical high-speed footage was recorded concurrently with the X-ray footage to provide context for each test. An example frame the optical camera is shown in Figure 5. The optical camera was synced to the X-ray camera and captured one frame for every five captured on the X-ray camera. Even with a lower temporal resolution, the optical high-speed camera was set with a wider field of view and continued to record after the X-ray shutters were closed to provide insight into the phenomena occurring in each test. As the X-ray beam is collimated and the camera viewing plane is orthogonal to the powder bed surface, the position of a printed line along the width of the powder bed cannot be deduced from the X-ray footage alone. However, as the optical high-speed camera is placed at an angle above the powder bed, context is given regarding the position of each printed line in the powder bed. The additional information provided by the optical high-speed camera serves as an important tool for interpreting the results from the X-ray footage.

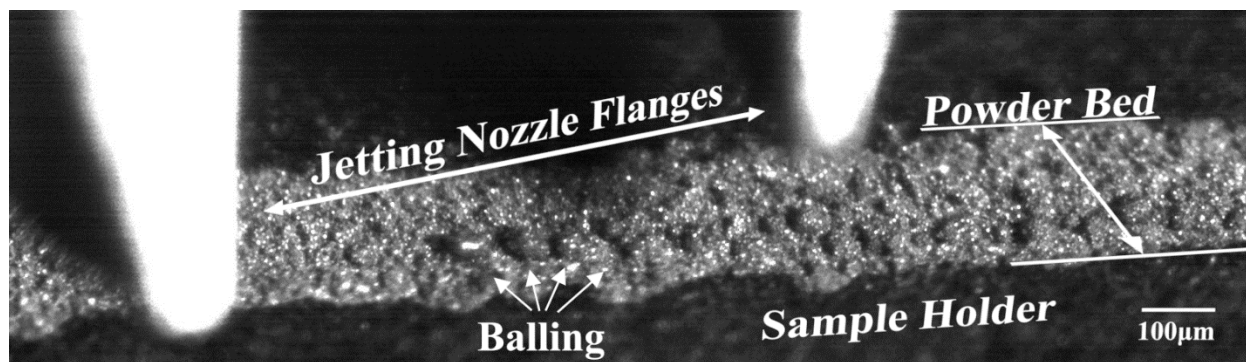


Figure 5. Example of a stainless steel sample in a 450 μ m wide glassy carbon sample holder during printing. The protective metal flanges of the jetting nozzle are visible above the sample.

Results and Discussion

Heating Effects

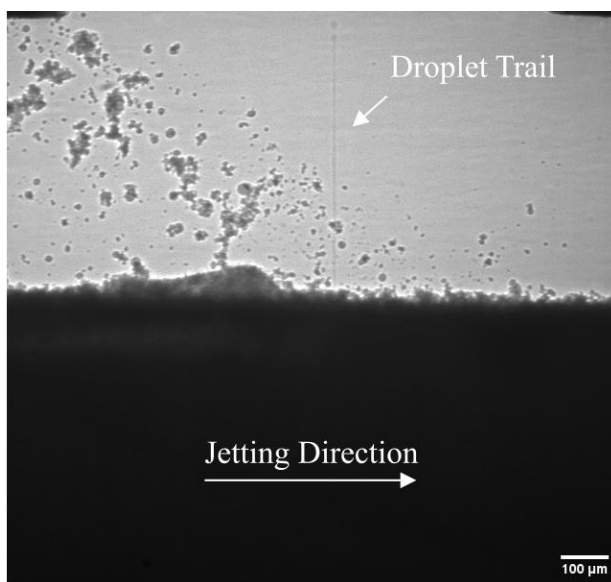


Figure 6. Excessive particle ejection likely due to evaporation of binder due to the X-ray energy absorbed by the stainless steel powder.

Figure 6 shows a frame captured by the X-ray camera. The sample was loose stainless steel 316L powder in a 450 μm wide glassy carbon sample holder. The undulator gap was set to 13mm and the exposure time was set to 0.8 μs . From the X-ray frame it can be immediately observed that there is insufficient X-ray transmission through the sample to observe subsurface phenomena. Additionally, an unexpectedly high amount of powder ejection was present during the print. Ejection occurred not only in reaction to binder droplet impact, but also in previously printed areas away from the droplet impact site. Additionally, there was observable unexpected change in trajectory of airborne powder particles. This was a clear indication that there was an undesirable phenomenon that was affecting testing.

Successive testing with newly prepared stainless steel samples revealed similar results. However, reducing X-ray intensity by increasing the undulator gap distances removed observable signs of the phenomena in question. Additionally, different materials such as silica glass beads did not exhibit this phenomenon. This led to the postulation that the phenomenon was caused by excessive heating of the stainless steel powder particles from absorption of the X-ray beam. The heating would cause moisture introduced into the powder bed from the aqueous binder to vaporize and cause unwanted powder rearrangement and ejection.

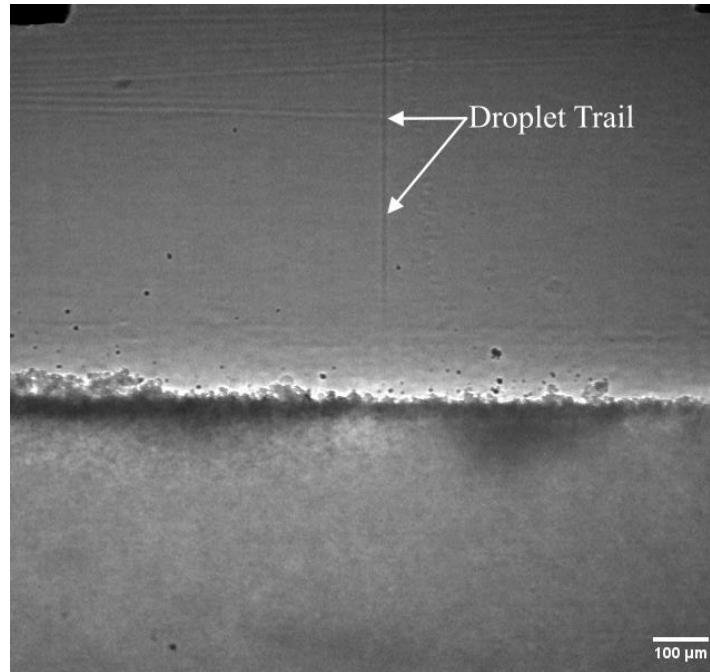


Figure 7. No observable heating effects. Subsurface visibility improved and droplet trail blurred from increased exposure time.

Figure 7 shows a similarly prepared stainless steel sample that did not exhibit any observable heating effects. The X-ray beam intensity was reduced by increasing the gap distance to 16.5mm. To compensate for reduced X-ray intensity and to increase subsurface visibility the exposure time was increased to 19 μ s. The significant increase in exposure time reduced the ability to resolve the binder droplet impact on the powder bed, but other interaction phenomena with larger time scales were still visible and heating effects were negated. In following tests, gap distance and exposure time were set with care to maximize temporal resolution and ability to resolve subsurface phenomena while avoiding heating effects.

While heating effects in future tests were largely avoided, the unwanted phenomenon would occasionally reemerge on lines printed close to the edge of the powder bed closest to the X-ray beam source. This is indicative of a thermal gradient in the powder bed along the X-ray beam propagation direction. Figure 8 shows frames from two tests printed on rolled stainless steel powder. Images were processed using flat-field correction described in the section on powder interaction depth. Tests were performed with an undulator gap of 18mm, an exposure time of 19 μ s, and line and droplet spacings of 50 μ m. The optical footage for these tests reveals that the line printed in Figure 8A was printed in the part of the powder bed furthest way from the X-ray source. No observable heating effects are present. The optical footage for the test shown in Figure 8B reveals that the line was printed closer to the X-ray source. Increased particle ejection likely due to heating effects is clearly visible.

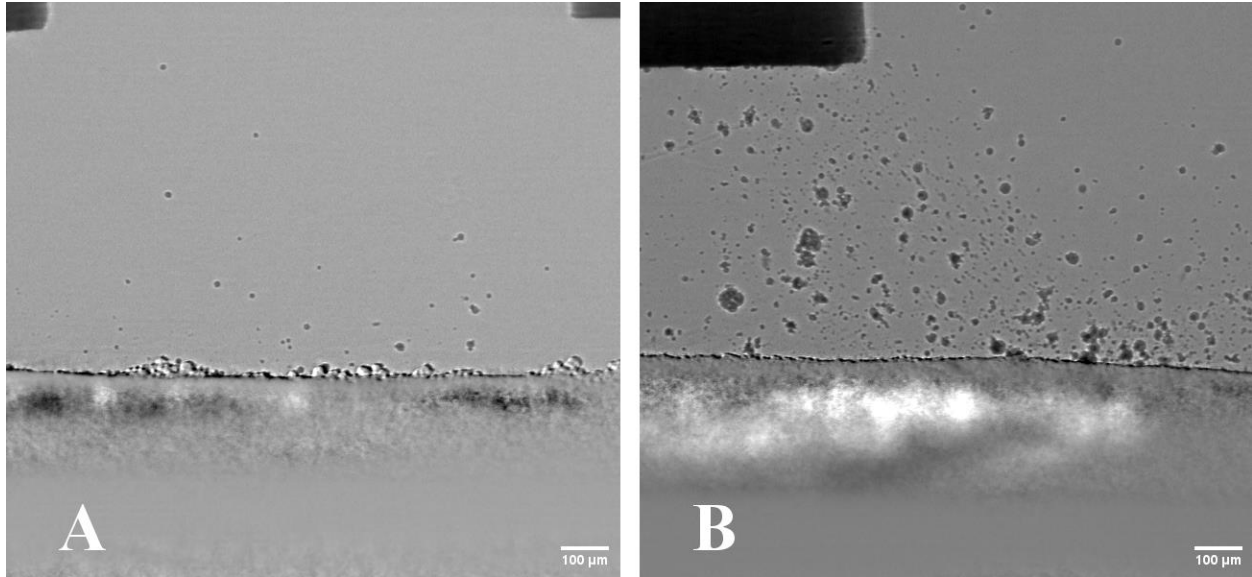


Figure 8. **A)** Line printed farther from the X-ray source, **B)** Line printed closer to the X-ray source. Lines were printed with 50 μ m droplet spacing in rolled stainless steel powder. Images were processed using flat-field correction.

Lowering X-ray beam intensity, increasing camera exposure time, and printing in the part of the powder bed furthest from the X-ray source proved to be effective methods for reducing visible heating effects while still being able to resolve subsurface phenomena. Tests that exhibited heating effects can be identified by excessive powder ejection away from the binder droplet impact site. Further analysis of results from tests with heating effects must be done with care, as the introduction of heating effects due to high-intensity X-rays does not represent industrially relevant conditions. Therefore, tests that exhibit heating effects may not provide meaningful insight into the fundamental phenomena present during the typical BJ process.

Powder Interaction Depth

A distinct advantage of high-speed X-ray imaging is *in situ* observation of binder-powder interaction below the powder bed surface. One way to quantify the subsurface interaction between the binder and powder is to measure the binder-powder interaction depth for each test. It should be noted that this interaction depth is not necessarily the same as binder penetration depth. The image processing technique used for measuring interaction depth relies on measuring the change in observed intensity of transmitted X-Rays in the powder bed during the duration of printing to identify regions of the powder bed that have undergone change in response to binder impact. A change in intensity in the powder bed between frames may be caused by densification or rarefaction of powder, introduction of additional material from the binder droplet, or other artifacts such as phase contrast halos or spatial and temporal intensity gradients of the X-ray beam.

Flat-field correction was used to reduce artifacts induced by variations in camera sensor sensitivity or X-ray intensity. Before performing a printing test, a series of images were captured similar to a printing test except that the jetting nozzle did not move, and no printing occurred. After printing, the images before printing could be used correct the printing images so that changes in observed intensity above and below the powder bed could be isolated. This flat-field corrected image sequence can be used for further processing to isolate the observed powder interaction depth.

Temporal median filtering can be applied after flat-field correction for further rejection of unwanted artifacts and isolation of changes in observed intensity that relate to interaction depth. Temporal median filtering involves computing a running median value of pixels between frames and subtracting that from the corrected footage. This serves to eliminate background elements and highlight motion in the recorded frames. Lastly, temporal projection can be used to combine the observed motion throughout the entire series of images into a single frame. In Figure 10A, the temporal projection filter generated the image by selecting the maximum pixel value among all frames in the image sequence for each pixel in the image. This projected image can be used to calculate an observed interaction depth.

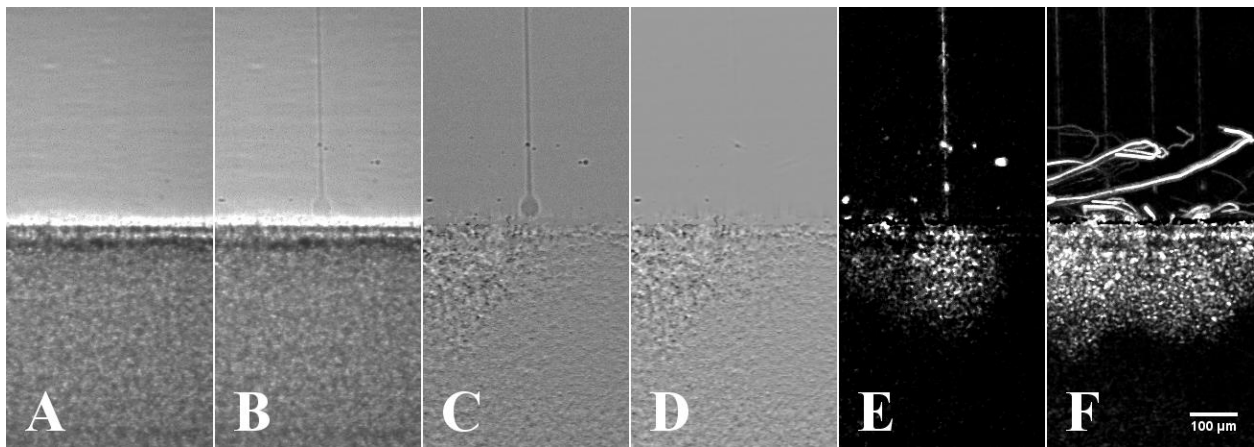


Figure 9. A) Flat, B) Print, C) Flat-field correction, D) Temporal median, E) Median filtered, F) Temporal projection

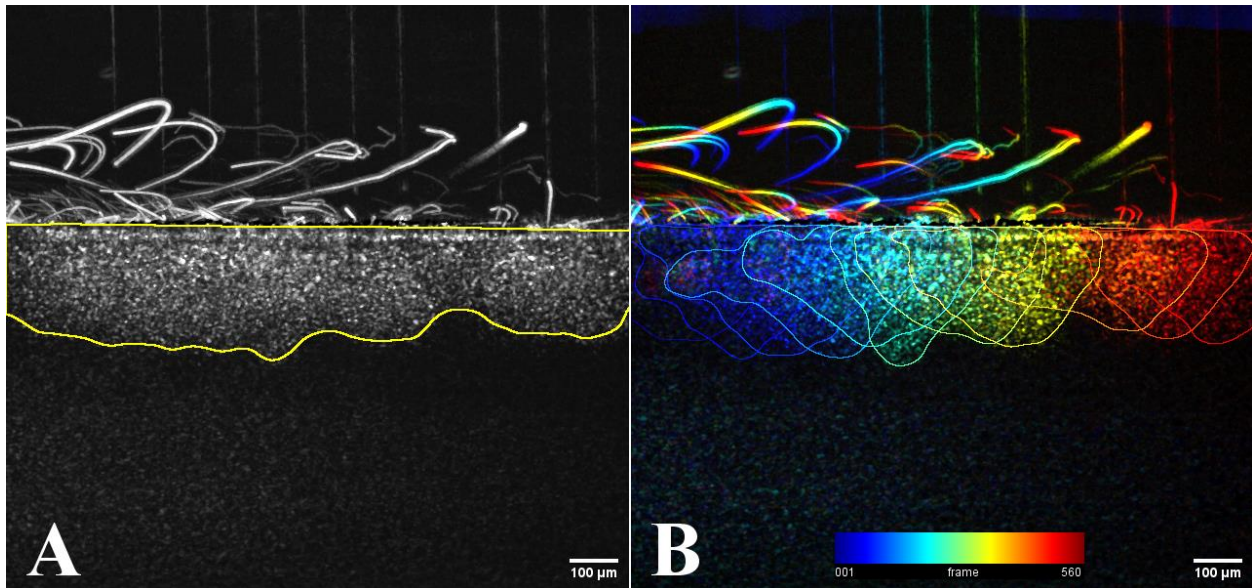


Figure 10. **A)** Temporal projection for measuring interaction depth, **B)** Color-coded temporal projection with outlines for calculated interaction profile for each binder droplet.

The average and variation of the observed interaction depth can be calculated from the subsurface profile and the line representing the powder bed. The interaction depth value can then be used to compare against tests conducted with different printing parameters to observe the impact of the printing parameters on the interaction depth.

An advantage of the temporal median filtering process is that it allows the ability to color code temporal projection, creating another method of visualizing the phenomena that occur during a test. Figure 10B shows a color-coded temporal projection where motion detected early in the video is colored blue and progresses towards red at the end of the video.

Additionally, the temporal projection filter can be set to process a subset of the frames captured during a test to target interaction effects of individual droplets. Figure 10B shows an outline of the calculated interaction depth for each binder droplet impact in the test. This technique can be used to compare the binder-powder interaction profiles for individual droplets in a single test and between tests as well as even calculate time scales for reaching full interaction depth after droplet impact.

Binder-powder interaction depth information for individual droplets, lines, and multiple lines is valuable information that provides insight into how powder below the powder bed surface react to droplet impact. Further analysis of how printing parameters affect interaction depth will lead to a better understanding of the fundamental phenomena that are responsible for BJ part defects formed in the printing process.

Powder Ejection

Another binder-powder interaction phenomenon observable using high-speed synchrotron X-ray imaging is powder particle ejection above the powder bed surface. As this phenomenon involves undesired rearrangement of powder and binder, observing particle ejection during the printing process may provide insight into defect formation in the BJ process. Optical observation of powder particles at needed temporal and spatial resolutions proves a challenge as optical setups typically have a narrow depth of focus, making particle detection and tracking difficult. The collimated X-ray beam allows for image capture with an extremely large depth of focus, ensuring that ejected powder particles stay in focus. Additionally, particle size can be accurately measured as apparent particle size is not affected by the particle position in the direction of the X-ray beam path. However, this means that particle motion in the direction of the X-ray beam cannot be accurately determined from the high-speed X-ray footage and only motion in the camera plane can be considered.

The color-coded temporal projection used when analyzing interaction depth is useful when analyzing powder ejection. Figure 11 shows a temporal projection from a rolled stainless steel sample printed with a 50 μm droplet spacing. Droplet impact sites show concentrated areas of powder ejection. Individual particles can also be tracked to estimate the number of ejected particles, particle size, and observed particle displacement. Figure 12 shows the same test as shown in Figure 11, but with individual particle tracking. Particle tracking allows observation of the first frame that each particle is detected, enabling plotting the number of ejected particles as a function of time. This metric can be used to compare ejection between tests. Additionally, particle speed can be estimated, noting that particle motion in the direction of the X-ray beam cannot be observed. This information can be used in conjunction with particle size to estimate the kinetic energy of ejected particles.

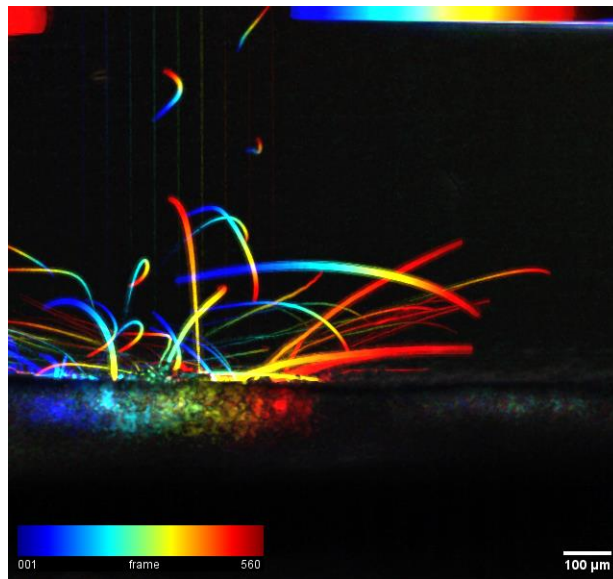


Figure 11. Color-coded temporal projection showing powder ejection from a line printed in rolled stainless steel powder.

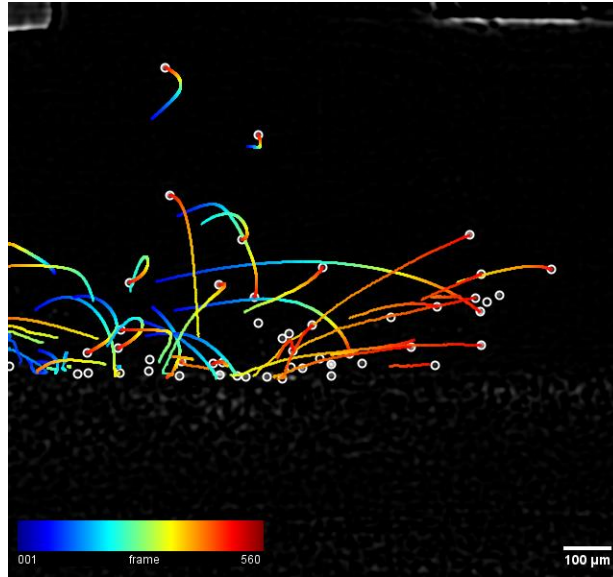


Figure 12. Particle tracking visualized in the same style as the color-coded projection.

Figure 13 shows a plot of number of ejected particles as a function of time for a loose spherical soda-lime glass powder bed. Five lines were printed with a droplet and line spacing of $40\mu\text{m}$. It can be noted that there is a reduction of the number of particles ejected for each of the lines succeeding line 1. This is indicative of a change in binder-powder interaction between printing on a dry powder bed and printing next to powder that has already been printed on. Further analysis is needed to confirm this trend for other droplet spacings and materials.

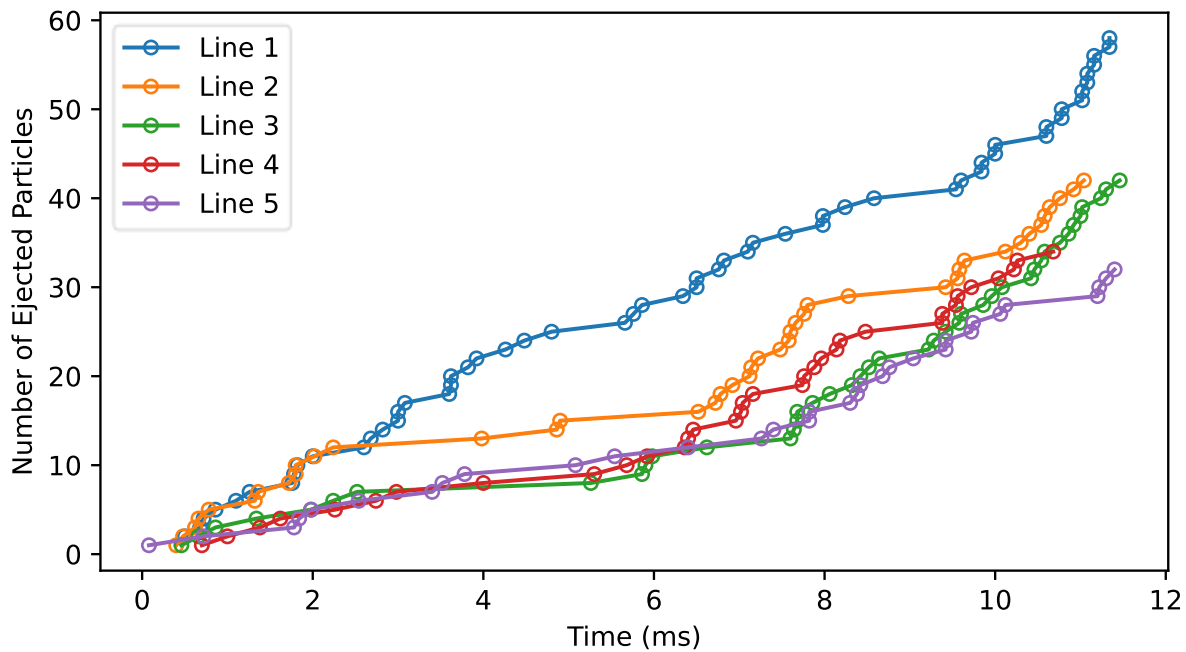


Figure 13. Number of particles as a function of time for each line printed in a loose soda-lime glass powder bed.

Figure 14 shows the number of ejected particles as a function of time for five lines printed in a rolled stainless steel powder bed. There is a gradual increase in ejected particles in lines 3 and 4 and a sharp increase in the number of ejected particles can be observed for line five. This is indicative of undesired heating effects impacting the test. The optical footage for line 5 confirms that the line was printed in the powder bed close to the X-ray source. Detecting large variations in number of ejected particles between tests can serve as a useful tool to identify when heating effects have occurred.

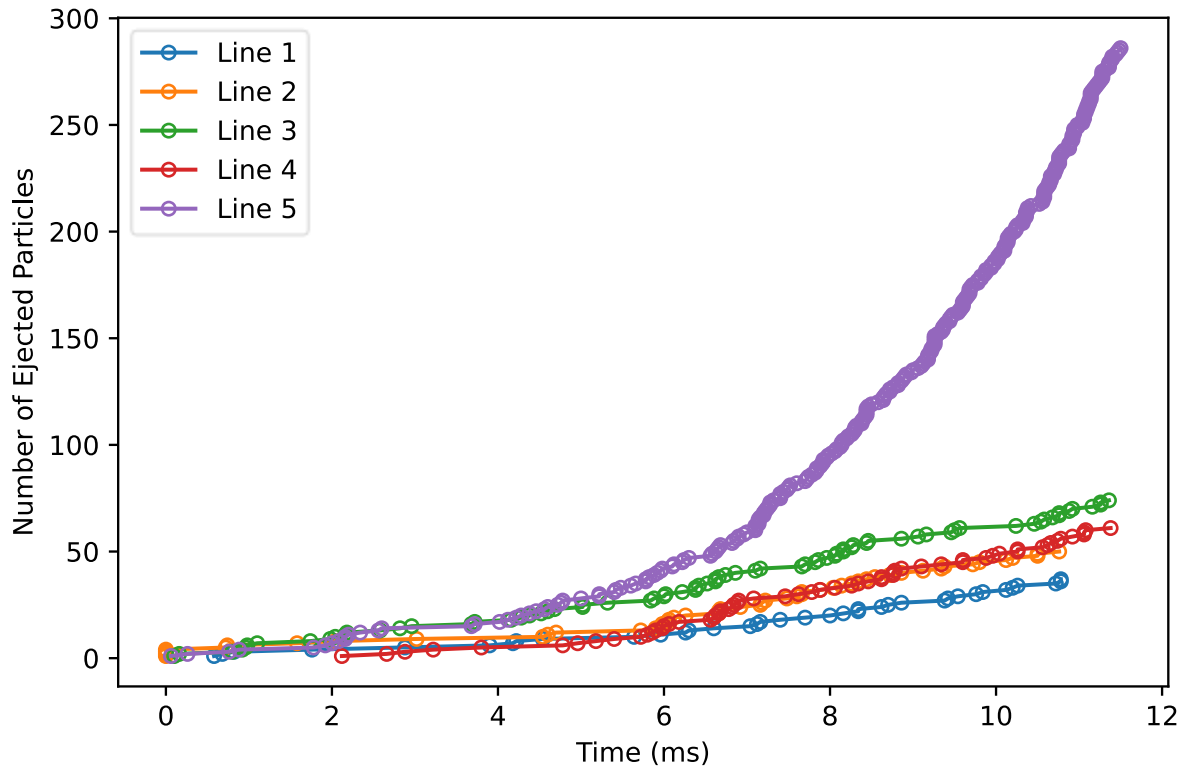


Figure 14. Number of particles as a function of time for each line printed in a rolled stainless steel powder bed. Heating effects are present on line 5.

Further analysis of the effect of printing parameters and materials on powder ejection will give insight into the fundamental phenomena present in the BJ process. Analyzing the testing footage to estimate the energy of droplet impact and powder ejection may help give understanding to what degree particle ejection is an elastic phenomenon. Additionally, tracking of ejected particles may show trends of printing parameters that lead to decreased particle ejection and result in less defect formation in the printing process.

Balling Formation

Another phenomenon that may influence defect formation in the BJ process that can be observed using high-speed synchrotron X-ray imaging is the formation of binder-powder agglomerates. These agglomerates represent significant transport of binder and powder which may lead to porous defects in a final part produced using BJ.

Figure 15 shows agglomerates formed from printing a line with 50 μm droplet spacing in loose stainless steel powder. Figure 16 shows the associated optical footage. An agglomerate was formed for every three droplets that impacted the powder bed, giving an approximate spacing of 150 μm between agglomerates. This matches the observations made by Parab, et al. [14]. Lighter regions in the image shown in Figure 15 below the powder bed surface may indicate regions where powder has been removed to form the agglomerates. These low density regions induced by agglomerate formation may be a mechanism for large pore formation in the BJ process.

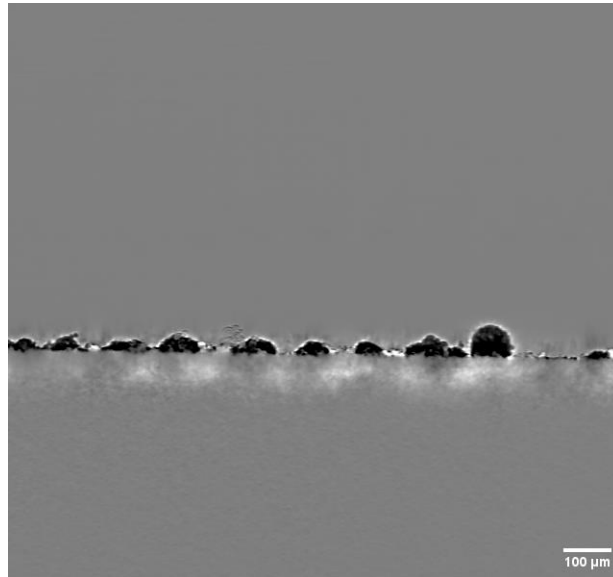


Figure 15. Agglomerate formation in a loose stainless steel powder bed. The line was printed with a 50 μm droplet spacing. The image was processed using flat-field correction.

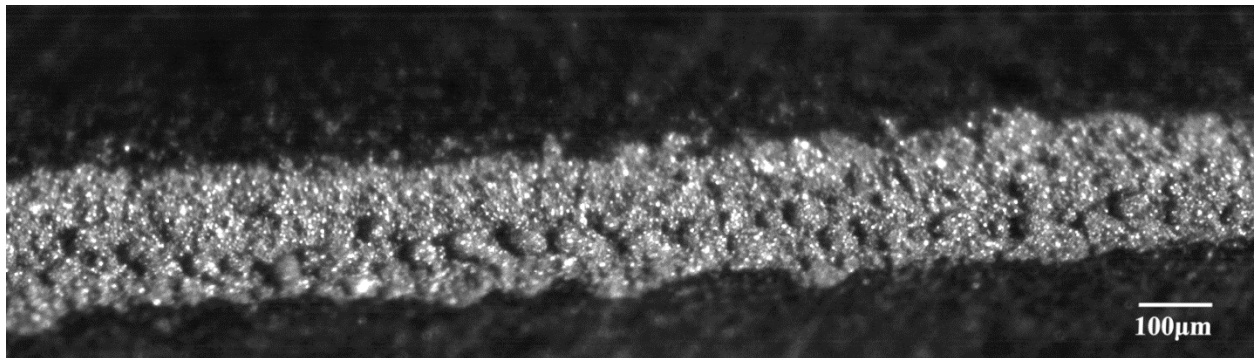


Figure 16. Optical footage showing agglomerate formation in a loose stainless steel powder bed.

Glass powder beds exhibited large airborne agglomerates that occasionally were impacted by successive binder droplets. Figure 17 shows such a case where large agglomerates can be seen above the powder bed which appears to have a large amount of material removed from the surface from formation of the agglomerates. This test was a first line printed with a 40 μ m droplet spacing in a loose soda-lime glass powder bed. This type of agglomerate formation only occurred when printing in glass powder with droplet spacings in the range of 40-60 μ m droplet spacings. Tests printed at lower droplet spacings did not exhibit visible agglomerates and those printed at higher droplet spacings showed smaller agglomerates forming on the powder bed surface. This indicates that there is a relationship between large agglomerate formation and droplet spacing.

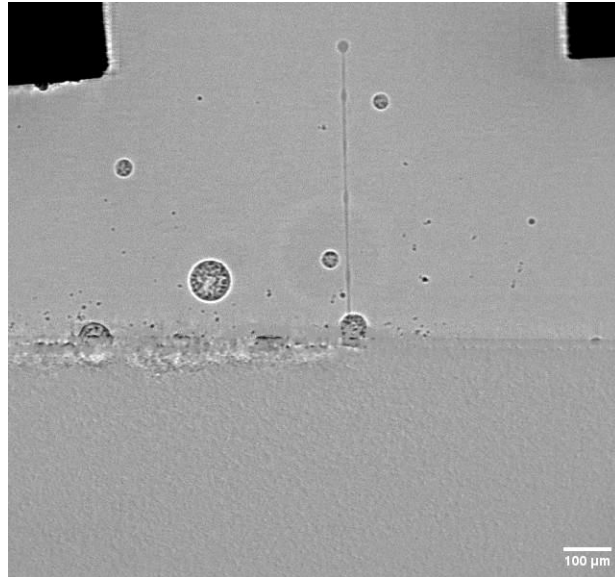


Figure 17. Large airborne agglomerates formed when printing a line with 40 μ m droplet spacing in a glass sphere powder bed. Image processed using flat-field correction.

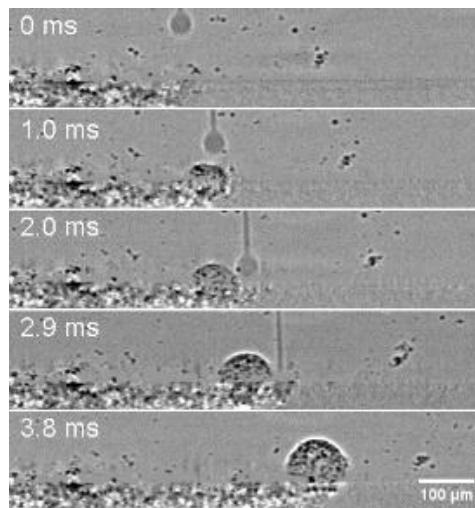


Figure 18. Large agglomerate formation when printing a line with 60 μ m droplet spacing. Consecutive droplets cause the agglomerate to roll forward and increase in size. Image processed using flat-field correction.

Figure 18 shows a sequence of images from a test of a line printed with a droplet spacing of 60 μ m in loose glass spheres. The frames show a phenomenon where the droplet impacts the forming agglomerate, causing it to roll forwards into the path of the next droplet. This causes the agglomerate to accumulate powder and binder, increasing in diameter. As the agglomerate rolls forward, a continuous track of disturbed powder is formed.

These large agglomerates displace significant amounts of binder and powder, creating regions of varying density in the powder bed. These defects may persist between layers and result in defects in a final printed part. The sensitivity of agglomerate formation to droplet spacing will be further analyzed to study the effect of the printing parameter on defect formation in printed parts. Comparison of agglomerate formation in consecutive lines may provide further insight into the phenomenon and the impact on final part defect formation. Additionally, future study on agglomerate formation could be conducted by using powders with added surfactants or adding surfactants in varying amounts to the binder to better understand parameters that affect agglomerate formation.

Conclusions

High-speed synchrotron X-ray imaging allows for *in situ* observation of the BJ process and the phenomena that are associated with part defect formation during the printing process. Observation of binder-powder interaction above and below the powder bed surface at high spatial and temporal resolutions enables analysis of phenomena such as binder droplet impact, subsurface powder interaction depth, particle ejection above the surface, and agglomerate formation. Care must be taken when selecting X-ray imaging parameters for X-ray absorbing materials such as stainless steel to avoid excessively heating the sample, thereby deviating from industrially relevant printing conditions.

The custom BJ system conducted tests with multi-line printing and varied droplet spacing. Initial analysis suggests powder ejection and powder bed density are affected by these printing parameters. Further analysis of the impact of tested printing parameters and observed phenomena may provide valuable insight into the fundamental mechanisms that generate print defects in the BJ process, inform existing numerical models, and indicate optimal printing parameters for reducing part defects.

Acknowledgments

This material is based upon work supported by the National Science Foundation through award number CMMI-1946724 and NRC 31310019M0006.

Disclaimer: Any opinions, findings, and conclusions or recommendations expressed in this material are those of the author(s) and do not necessarily reflect the views of the National Science Foundation.

This research used resources of the Advanced Photon Source, a U.S. Department of Energy (DOE) Office of Science user facility operated for the DOE Office of Science by Argonne National Laboratory under Contract No. DE-AC02-06CH11357.

References

- [1] E. Sachs, M. Cima, P. Williams, D. Brancazio, J. Cornie, Three Dimensional Printing: Rapid Tooling and Prototypes Directly from a CAD Model, *Journal of Engineering for Industry*, 114 (1992) 481-488.
- [2] M. Ziaee, N.B. Crane, Binder jetting: A review of process, materials, and methods, *Additive Manufacturing*, 28 (2019) 781-801.
- [3] I.a. Gibson, D.a. Rosen, B.a. Stucker, *Additive manufacturing technologies : 3D printing, rapid prototyping, and direct digital manufacturing*, Second edition. ed., Springer, New York, NY, 2015.
- [4] M. Li, W. Du, A. Elwany, Z. Pei, C. Ma, Metal Binder Jetting Additive Manufacturing: A Literature Review, *Journal of Manufacturing Science and Engineering*, 142 (2020) 1-45.
- [5] E. Sachs, M. Cima, J. Bredt, A. Curodeau, T. Fan, D. Brancazio, CAD-casting: direct fabrication of ceramic shells and cores by three dimensional printing, *Manufacturing Review*, 5 (1992) 117-126.
- [6] J. Moon, J.E. Grau, V. Knezevic, M.J. Cima, E.M. Sachs, Ink-jet printing of binders for ceramic components, *Journal of the American Ceramic Society*, 85 (2002) 755-762.
- [7] D. Huson, 3D printed ceramics: Current challenges and future potential, in: 32nd International Conference on Digital Printing Technologies, NIP 2016, September 12, 2016 - September 16, 2016, Society for Imaging Science and Technology, Manchester, United kingdom, 2016, pp. 374-377.
- [8] T. Sivarupan, N. Balasubramani, P. Saxena, D. Nagarajan, M. El Mansori, K. Salonitis, M. Jolly, M.S. Dargusch, A review on the progress and challenges of binder jet 3D printing of sand moulds for advanced casting, *Additive Manufacturing*, 40 (2021).
- [9] H. Miyanaji, S. Zhang, L. Yang, A new physics-based model for equilibrium saturation determination in binder jetting additive manufacturing process, *International Journal of Machine Tools and Manufacture*, 124 (2018) 1-11.
- [10] Y. Bai, C. Wall, H. Pham, A. Esker, C.B. Williams, Characterizing Binder-Powder Interaction in Binder Jetting Additive Manufacturing Via Sessile Drop Goniometry, *J. Manuf. Sci. Eng.-Trans. ASME*, 141 (2019) 11.
- [11] T. Colton, N.B. Crane, Influence of droplet velocity, spacing, and inter-arrival time on line formation and saturation in binder jet additive manufacturing, *Additive Manufacturing*, 37 (2021).
- [12] T. Colton, C. Inkley, A. Berry, N.B. Crane, Impact of inkjet printing parameters and environmental conditions on formation of 2D and 3D binder jetting geometries, *Journal of Manufacturing Processes*, 71 (2021) 187-196.
- [13] N.B. Crane, Impact of part thickness and drying conditions on saturation limits in binder jet additive manufacturing, *Additive Manufacturing*, 33 (2020) 101127.

- [14] N.D. Parab, J.E. Barnes, C. Zhao, R.W. Cunningham, K. Fezzaa, A.D. Rollett, T. Sun, Real time observation of binder jetting printing process using high-speed X-ray imaging, *Scientific Reports*, 9 (2019) 2499.
- [15] T. Hua, Three-dimensional simulation of micrometer-sized droplet impact and penetration into the powder bed, *Chemical Engineering Science*, 153 (2016) 93-107.
- [16] H. Kang, S.D.N. Lourenço, W.M. Yan, Lattice Boltzmann simulation of droplet dynamics on granular surfaces with variable wettability, *Physical Review E*, 98 (2018).
- [17] W. Yuanyuan, J. Pengfei, Y. Weidong, P. Kai, Z. Sixiang, Simulation and experimental study of binder droplet infiltration in 3DP technology, *Modern Physics Letters B*, 32 (2018) 1850272 (1850220 pp.).